The Astrophysical Journal, 893:95 (14pp), 2020 April 20 https://doi.org/10.3847/1538-4357/ab7eb8

Spectroscopy of Broad Absorption Line Quasars at $3 \lesssim Z \lesssim 5$. I. Evidence for Quasar Winds Shaping Broad/Narrow Emission Line Regions

Weimin Yi[1,2,3], Wenwen Zuo[4], Jinyi Yang[5], Feige Wang[5], John Timlin[2], Catherine Grier[5], Xue-Bing Wu[6,7], Xiaohui Fan[5], and Jin-Ming Bai[1,3]
[1] Yunnan Observatories, Kunming, 650216, People's Republic of China; ywm@ynao.ac.cn
[2] Department of Astronomy & Astrophysics, The Pennsylvania State University, 525 Davey Lab, University Park, PA 16802, USA
[3] Key Laboratory for the Structure and Evolution of Celestial Objects, Chinese Academy of Sciences, Kunming 650216, People's Republic of China
[4] Shanghai Astronomical Observatory, Shanghai 200030, People's Republic of China
[5] Steward Observatory, The University of Arizona, 933 North Cherry Avenue, Tucson, AZ 85721-0065, USA
[6] Kavli Institute for Astronomy and Astrophysics, Peking University, Beijing 100871, People's Republic of China
[7] Department of Astronomy, Peking University, Yi He Yuan Lu 5, Hai Dian District, Beijing 100871, People's Republic of China
Received 2019 November 15; revised 2020 March 5; accepted 2020 March 7; published 2020 April 20

Abstract

We present an observational study of 22 broad absorption line quasars (BAL QSOs) at $3 \lesssim z \lesssim 5$ based on optical/near-IR spectroscopy, aiming to investigate quasar winds and their effects. The near-IR spectroscopy covers the Hβ and/or Mg II broad emission lines (BELs) for these quasars, allowing us to estimate their central black hole (BH) masses in a robust way. We found that our BAL QSOs, on average, do not have a higher Eddington ratio than that from non-BAL QSOs matched in redshift and/or luminosity. In a subset consisting of seven strong BAL QSOs possessing subrelativistic BAL outflows, we see the prevalence of large C IV BEL blueshift ($\sim$3100 km s^{-1}) and weak [O III] emission (particularly the narrow [O III] λ5007 component), indicative of nuclear outflows affecting the narrow emission line (NEL) regions. In another subset consisting of 13 BAL QSOs having simultaneous observations of Mg II and Hβ, we found a strong correlation between 3000 and 5000 Å monochromatic luminosity, consistent with that from non-BAL QSOs matched in redshift and luminosity; however, there is no correlation between Mg II and Hβ in FWHM, likely due to nuclear outflows influencing the BEL regions. Our spectroscopic investigations offer strong evidence that the presence of nuclear outflows plays an important role in shaping the BEL/NEL regions of these quasars and, possibly, regulating the growth of central supermassive BHs. We propose that BEL blueshift and BALs could be different manifestations of the same outflow system viewed at different sight lines and/or phases.

Unified Astronomy Thesaurus concepts: Quasars (1319); Broad-absorption line quasar (183); Supermassive black holes (1663)

1. Introduction

Broad absorption line quasars (BAL QSOs; Weymann et al. 1991) consist of about 20% of the quasar population before correcting selection effects and up to $\sim$40% after correction (e.g., Hewett & Foltz 2003; Trump et al. 2006; Gibson et al. 2009; Allen et al. 2011). The BALs are unambiguous quasar winds and provide abundant diagnostics for observational studies of intrinsic outflows from low to high redshifts via X-ray, UV, optical, and IR spectroscopy. In general, most BAL QSOs are characterized by high-ionization BALs (HiBALs). In addition to HiBALs, a small fraction ($\sim$10%; e.g., Trump et al. 2006) of the BAL population also shows absorption troughs characterized by low-ionization species (e.g., Mg II and Al III) in their spectra, which are classified as LoBALs. An even rarer type of BAL QSO shows prominent Fe II and Fe III absorption in addition to other low-ionization species, namely FeLoBALs.

The BAL phenomena are widely interpreted by either an orientation or evolution effect. The orientation scenario appears to be plausible for most HiBALs due to their similar continuum and emission line properties (e.g., Weymann et al. 1991; Reichard et al. 2003a). However, spectropolarimetry studies suggest that BAL QSOs may not simply be normal quasars seen from an edge-on perspective (e.g., DiPompeo et al. 2010). The evolution scenario has often been proposed for interpreting the phenomena of (Fe)LoBALs,[8] as they are often found from far-IR luminous and high star formation objects (e.g., Becker et al. 2000; Farrah et al. 2010). In addition, Gallerani et al. (2010) found systematic differences between BAL and non-BAL QSOs regarding observational properties that should be isotropic. Therefore, BAL QSOs might be used to investigate the early stage of quasar evolution (Boroson & Green 1992; Voit et al. 1993; Becker et al. 2000; Gallerani et al. 2010). In this picture, a LoBAL QSO may be a young active galactic nucleus (AGN) in a short-lived transition phase between an ultraluminous infrared galaxy and a normal unobscured quasar, in which the quasar is experiencing a high-accretion process and blows off the dust envelope by powerful outflows. As a consequence, such outflows may quench star formation in the host galaxy (Farrah et al. 2012; Faucher-Giguère et al. 2012).

Systematic studies of large BAL QSO samples have greatly improved our understanding of BAL structures, dynamics, and intrinsic physics in both high- and low-ionization species (e.g., Reichard et al. 2003b; Gibson et al. 2009; Schulze et al. 2017; Hamann et al. 2019). The BAL QSOs usually exhibit redder continua compared with non-BAL QSOs, which is often interpreted as stronger reddening by dust in the circumnuclear region (e.g., Brotherton et al. 2001; Reichard et al. 2003a).

[8] Hereafter, we use (Fe)LoBAL to represent a sample including both FeLoBAL and LoBAL types.

Table 1
Near-IR Spectroscopic Studies of BAL QSOs at $z \gtrsim 3$

Reference	Redshift	R	Num.
Maiolino et al. (2004)	$4.9 < z < 6.2$	~50	4
Gallerani et al. (2010)	$3.9 < z < 6.2$	50–800	11
Yi et al. (2017)	$z = 4.82$	~350	1
Wang et al. (2018)	$z = 7.02$	~4000	1
This work	$2.5 < z < 5.1$	~2700	22

Note. The fourth column represents the number of BAL QSOs, and R is the spectral resolution.

There is, however, an obvious deficiency of sample investigations of higher-redshift BAL QSOs based on UV/optical spectroscopy in the rest frame (see Table 1), leading to a poor understanding of the BAL population in the early universe. The extinction curve of BAL QSOs at $z > 4$, based on two dedicated studies (Maiolino et al. 2004; Gallerani et al. 2010), likely deviates from the SMC extinction curve, supporting the argument of an evolutionary explanation for reddened BAL QSOs at high redshift. Specifically, the dust production mechanism in the early universe may differ from that at low or intermediate redshift. However, the above two studies of high-z BAL QSOs focused primarily on the investigation of internal extinction and did not estimate black hole (BH) masses in their samples (they were also limited by their low-resolution spectra; see Table 1).

At high redshift, the single-epoch spectral relation is often adopted to investigate supermassive black holes (SMBHs) residing in QSOs (e.g., McLure & Dunlop 2004; Vestergaard & Peterson 2006). In this relation, broad emission lines (BELs), such as Hβ, Hα, and Mg II, are considered to be better BH mass estimators than the C IV emission line. Since BAL QSOs have strong reddening and absorption, which directly affects either the BELs or the neighboring continuum, previous sample investigations of SMBHs in high-redshift QSOs are exclusively based on non-BAL QSOs (e.g. Coatman et al. 2017; Jiang et al. 2007; Netzer et al. 2007; Trakhtenbrot et al. 2011; López et al. 2016; Zuo et al. 2015). Recently, a dedicated spectroscopic study based on a sample of 22 LoBAL QSOs at $1 < z < 2.5$ revealed that line profiles of Hβ and Hα are little affected by absorption (Schulze et al. 2017), indicating that they can serve as BH mass estimators for BAL QSOs. Particularly, the spectral region around the Hα or Hβ BEL is much less affected by intrinsic reddening and absorption compared to that around the C IV or Mg II BEL. Therefore, the Balmer (Hα or Hβ) BELs provide unique and valuable diagnostics for the investigation of central engines powering BAL QSOs.

In this work, we present observational results from a sample including 22 BAL QSOs at $3 \lesssim z \lesssim 5$ based on optical/near-IR spectroscopy. The majority of optical spectra in the sample are collected from the Sloan Digital Sky Survey (SDSS), with a few complemented by other telescopes. We have obtained near-IR spectra for all quasars in the sample through the Telescope Access Program (TAP) from the Chinese Academy of Sciences, which allows us to (1) estimate luminosity, BH mass, and Eddington ratio for the sample; (2) systematically compare with non-BAL QSOs matched in redshift and/or luminosity; and (3) investigate nuclear outflows and their effects at high redshift. Throughout this paper, a flat cosmology with $H_0 = 70\,\mathrm{km\,s^{-1}Mpc^{-1}}$, $\Omega_M = 0.3$, and $\Omega_\Lambda = 0.7$ is adopted unless stated otherwise.

2. Sample Selection and Observation

2.1. Sample Selection

We began by searching for luminous BAL QSOs from the DR12 quasar catalog (Pâris et al. 2017) with absorption index (AI; see Pâris et al. 2017) (C IV) $\gtrsim 8000\,\mathrm{km\,s^{-1}}$ at $z > 4.3$. To reliably measure the trough width and depth, quasars with apparent overlapping troughs and heavy reddening imprinted on the blueward of the C IV emission line were excluded. Four BAL QSOs remained after this selection. We also include two more newly discovered BAL QSOs at $z > 4$ that were reported by recent studies (Yi et al. 2015; Wang et al. 2016).

Due to the rarity of high-AI (C IV) BAL QSOs at $z > 4$, we added six BAL QSOs showing relatively strong BAL troughs ($2000\,\mathrm{km\,s^{-1}} < \mathrm{AI} < 8000\,\mathrm{km\,s^{-1}}$) and five comparison BAL QSOs with weak BAL troughs ($\mathrm{AI} < 2000\,\mathrm{km\,s^{-1}}$) at $2.5 < z < 4$ to our sample. Considering strong telluric absorption windows in the near-IR wavelengths (i.e., 1.35–1.45 and 1.8–1.9 μm), a proper redshift cut was made to keep the Mg II and/or Hβ emission lines away from these windows. In total, this includes 11 BAL QSOs at $2.5 < z < 4$. Together with the six BAL QSOs at $4.3 < z < 5$ from the first stage and another five BAL QSOs at $3 < z < 4$ from Zuo et al. (2015), our final sample consists of 22 BAL QSOs with newly and previously obtained near-IR spectra.

The basic descriptions of these BAL QSOs are tabulated in Table 2, where most of these measurements are retrieved from Pâris et al. (2017). The systemic redshift values are determined by the [O III], Hβ, or Mg II lines from near-IR spectra, depending on their appearance. We visually inspected all spectra before performing quantitative measurements. We identified 12 LoBAL QSOs in this sample. Another three cannot be identified due to low signal-to-noise ratio (S/N) spectra and/or an incapability of identifying LoBALs in strong telluric absorption windows. The LoBAL fraction, therefore, is 54.5% (12/22) or potentially higher due to unidentifiable LoBALs. We do note that this high fraction is likely caused by our preference in selecting strong BAL QSOs to construct the sample.

2.2. Compilation of Optical Data

Our optical spectra in the sample are primarily obtained from the DR14 SAS website[9] by matching the coordinates of the selected BAL QSOs to source positions within a 3″ tolerance. These spectra are corrected for calibration errors that result from atmospheric differential refraction and fiber offsets during observations (see Margala et al. 2016 for details).

Additional optical spectroscopic observations were carried out during several runs from 2015 to 2018 using the Yunnan Faint Object Spectrograph and Camera mounted on the Lijiang 2.4 m telescope (LJT/YFOSC; Fan et al. 2015). The FWHM of the YFOSC imaging data varies mostly in the range from 1.″0 to 2.″5; we thus chose a slit of 1.″8 for the spectroscopic observations. Each night the neon/helium arc lamps were taken for wavelength calibration and a spectrophotometric standard star was observed, followed by the target at similar airmass and position. All of the calibration data, including bias, sky flat fields, and internal lamp flats, were obtained at the beginning/end of each observing night. The data reduction was performed

[9] https://dr14.sdss.org/optical/spectrum/search

Table 2
C IV BAL Properties of 22 BAL QSOs in the Sample

Name	R.A. (J2000)	Decl. (J2000)	AI (C IV) (km s^{-1})	$v_{\rm min}$ (km s^{-1})	$v_{\rm max}$ (km s^{-1})	$v_{\rm cen}$ (km s^{-1})	EW (Å)	$d_{\rm BAL}$	z	Type
014049.18−083942.5	25.20492	−8.66181	1760 ± 12	23134	28496	25857	11.9 ± 0.3	0.42	3.717	Hi
015048.83+004126.2	27.70346	0.69061	538 ± 4	2913	4005	3470	3.4 ± 0.2	0.57	3.701	Hi
021646.94−092107.3	34.19561	−9.35204	2697 ± 15	11695	23009	13740	19.4 ± 0.6	0.58	3.732	Hi
074628.70+301419.0 ♦	116.61961	30.23863	11060 ± 45	7016	30120	9600	68.1 ± 0.7	0.81	3.173	Lo
APM08279	127.92375	52.75486	1276 ± 97	4125	10607	7587	10.0 ± 0.9	0.29	3.911	Hi
083718.63+482806.5	129.32764	48.46848	8068 ± 48	2645	15299	8141	48.3 ± 0.4	0.73	3.64	Lo
084401.95+050357.9 ♦	131.00813	5.06608	9173 ± 60	4656	28197	13935	59.2 ± 0.5	0.48	3.36	Lo
091935.36+193834.7	139.89737	19.64297	13189 ± 80	1077	22360	10304	79.2 ± 0.6	0.71	3.541	Lo
103256.70+514014.5	158.23628	51.6707	11018 ± 66	1231	27751	9989	69.6 ± 0.7	0.62	3.925	Lo?
115023.57+281907.4	177.59825	28.31875	788 ± 5	1109	2549	1832	4.92 ± 0.3	0.63	3.12	Hi
120447.15+330938.7 ♦	181.19647	33.16077	12430 ± 76	6048	29166	16577	76.3 ± 0.5	0.63	3.652	Lo
121027.62+174108.9 ♦	182.61508	17.68581	6484 ± 87	14122	29000	20965	41.8 ± 0.7	0.5	3.831	Lo
123754.82+084106.7	189.47844	8.68522	2938 ± 18	1612	6109	3710	17.5 ± 0.3	0.74	2.897	Hi
125958.72+610122.9	194.99469	61.02303	478 ± 3	3375	4941	4238	3.76 ± 0.2	0.39	3.572	Hi
141546.24+112943.4	213.94267	11.49540	4896 ± 32	3209	13804	7533	31.3 ± 0.3	0.56	2.556	Lo
150332.17+364118.0	225.88404	36.68833	4387 ± 20	3924	28213	5232	32.3 ± 0.6	0.76	3.261	Lo
012247.34+121624.0 ♦	20.69730	12.27330	14360 ± 1900	5886	30479	14438	76.1 ± 8.9	0.68	4.82	Lo
092819.28+534024.1 ♦	142.08037	53.67337	9711 ± 49	8035	27634	9445	59.7 ± 0.8	0.85	4.47	Lo
104846.63+440710.7 ♦	162.19431	44.11966	12258 ± 74	4820	25899	13520	74.3 ± 0.6	0.67	4.39	Lo
133529.45+410125.9	203.87271	41.02388	5143 ± 32	16436	26873	20803	32.0 ± 0.4	0.59	4.3	Lo
151035.29+514841.0	227.64705	51.81141	6790 ± 28	5160	21578	5749	43.0 ± 2	0.77	5.096	Lo?
163810.38+150058.2	249.54325	15.01617	5030 ± 29	21700	32700	26850	31.7 ± 3	0.55	4.84	Lo?

Note. Here $v_{\rm cen}$ is a flux-weighted centroid velocity in the C IV BAL trough; $v_{\rm min}$ and $v_{\rm max}$ are the corresponding minimum and maximum velocities, respectively; EW is the equivalent width; and $d_{\rm BAL}$ is the average depth across the entire C IV BAL trough. Hi/Lo represent high-/low-ionization BALs, respectively. The filled diamonds indicate the seven QSOs with relatively high S/N and $v_{\rm min}>$ 3000 km s^{-1} that are used to produce the composite spectra of strong BAL QSOs (see Section 3.5). The Lo? symbol represents an unidentifiable LoBAL due to the lack of wavelength coverage or strong contamination from telluric absorption.

by IRAF packages following standard reduction steps for bias/sky subtractions, flat-fielding correction, and flux calibration.

2.3. Near-IR Spectroscopic Observations and Data Reduction

The near-IR spectroscopic observations of all objects tabulated in Table 2 were carried out with the TripleSpec spectrograph (Wilson et al. 2004) at the Palomar Hale 200 inch telescope (P200/TripleSpec; Wilson et al. 2004). TripleSpec provides a wide wavelength coverage from 0.95 to 2.46 μm at an average spectral resolution of $R \sim 2700$, allowing simultaneous observations in the *JHK* bands. A high Fowler depth ($6 \sim 10$) is set for faint objects to optimize the readout noise after each single exposure. A slit width of 1″ and the ABBA dither pattern along the slit were chosen to improve the sky subtraction for all targets throughout these observational runs. Total exposure times varied between 24 and 60 minutes, depending on the apparent magnitudes and weather conditions. During each night, several telluric A0V standard stars were observed at a similar airmass compared to that of the target.

The data reduction for the spectroscopic data from TripleSpec is performed using the modified IDL-based Spextool3 package (Cushing et al. 2004), as described in detail from Zuo et al. (2015). The standard process includes sky background subtraction, flat-field correction, wavelength identification, and telluric correction. Based on the reduced near-IR spectra, we determine systemic redshift using the [O III], Hβ, or Mg II emission lines, ordered by descending priority when available.

2.4. Notes on Individual Objects

The object J0122+1216 was discovered as a quasar using the Lijiang 2.4 m telescope (Yi et al. 2015) in optical spectroscopy; later, it was further identified as a LoBAL QSO at $z = 4.82$ using near-IR spectroscopy (Yi et al. 2017). Recently, this LoBAL QSO was investigated by Jeon et al. (2017), where their measurements of the luminosity and BH mass are consistent with those from Yi et al. (2017). As the quality of near-IR spectra obtained by the Magellan telescope (see Jeon et al. 2017) is much higher than that from Yi et al. (2017), we use their near-IR spectra (in private communication) for J0122+1216 in this work.

One of the brightest quasars is APM 08279; its brightness is due to gravitational lensing (Irwin et al. 1998). Another lensed quasar showing a "cloverleaf" structure (Magain et al. 1988) is J1415+1129. Since previous studies reported a wide range of possible magnification factors (4–100) for this quasar, for simplicity, we choose to use the bolometric luminosity, assuming that it is equal to the Eddington luminosity limit.

3. Spectroscopic Measurements and Analyses

We use several different methods to obtain more reliable measurements based on optical/near-IR spectroscopic/photometric data. In particular, we focus on redshift determination, similar spectral shape matching at close redshifts, continuum fitting, correction of absolute spectral flux, and emission line fitting. The relevant measurements are tabulated in Tables 2 and 3.

Table 3
Spectral Measurements and Derived BH Properties Based on P200/TripleSpec Observations

Name SDSS J	$\mathrm{FWHM_{MgII}}$ (km s^{-1})	$\log L_{3000\,\text{Å}}$ (erg s^{-1})	$\mathrm{FWHM_{H\beta}}$ (km s^{-1})	$\log L_{5100}$ (erg s^{-1})	$\mathrm{FWHM_{[O\,III]}}$ (km s^{-1})	$\log L_{\mathrm{bol}}$ (erg s^{-1})	$\log M_{\mathrm{BH}}$ ($M_\odot$)	$\log \lambda_{\mathrm{Edd}}$
0140−0839	4735 ± 2430	47.25 ± 0.01	5348 ± 697	46.99 ± 0.01	1870 ± 500	47.96 ± 0.01	9.86 ± 0.11	−0.02 ± 0.12
0150+0041	5668 ± 105	46.95 ± 0.01	5225 ± 780	46.74 ± 0.01	1410 ± 80	47.71 ± 0.01	9.38 ± 0.12	0.01 ± 0.13
0216−0921	2550 ± 650	46.99 ± 0.03	3729 ± 80	46.77 ± 0.03	⋯	47.74 ± 0.01	9.38 ± 0.03	0.25 ± 0.05
0746+3014	4517 ± 2078	47.13 ± 0.09	7018 ± 900	46.90 ± 0.01	1300 ± 360	47.87 ± 0.01	10.05 ± 0.19	−0.29 ± 0.19
APM 08279	⋯	⋯	5020 ± 38	46.92 ± 0.5	⋯	47.89 ± 0.5	9.80 ± 0.30	0.001 ± 0.30
0837+4828	4244 ± 260	46.83 ± 0.08	5197 ± 1630	46.63 ± 0.03	1436 ± 240	47.59 ± 0.03	9.65 ± 0.25	−0.17 ± 0.23
0844+0503	3850 ± 830	47.44 ± 0.01	5812 ± 35	47.25 ± 0.01	2100 ± 90	48.21 ± 0.01	10.06 ± 0.01	0.03 ± 0.03
0919+1938	3800 ± 1690	46.82 ± 0.1	5214 ± 380	46.70 ± 0.03	1400 ± 690	47.67 ± 0.03	9.70 ± 0.07	−0.14 ± 0.11
1032+5140	⋯	⋯	3193 ± 820	46.63 ± 0.02	⋯	47.59 ± 0.02	9.23 ± 0.21	0.25 ± 0.32
1150+2819	6024 ± 5450	47.24 ± 0.02	4071 ± 60	47.02 ± 0.02	1069 ± 35	47.99 ± 0.02	9.64 ± 0.02	0.24 ± 0.04
1204+3309	4928 ± 188	46.93 ± 0.04	5785 ± 165	46.88 ± 0.02	1400 ± 560	47.84 ± 0.02	9.87 ± 0.03	−0.14 ± 0.04
1210+1741	⋯	⋯	6476 ± 960	47.07 ± 0.01	⋯	48.04 ± 0.01	10.07 ± 0.04	−0.14 ± 0.05
1237+0841	4840 ± 2030	47.10 ± 0.01	⋯	⋯	⋯	47.81 ± 0.01	9.77 ± 0.4	−0.07 ± 0.4
1259+6101	2400 ± 4000	46.99 ± 0.01	5540 ± 2250	46.83 ± 0.01	1680 ± 310	47.80 ± 0.01	9.81 ± 0.22	−0.13 ± 0.24
1415+1129	4593 ± 900	46.71 ± 0.03	3915 ± 125	46.49 ± 0.03	1390 ± 86	47.46 ± 0.03	9.66 ± 0.05	0.002 ± 0.18
1503+3641	3428 ± 820	47.20 ± 0.02	5336 ± 62	46.88 ± 0.02	1387 ± 86	47.85 ± 0.02	9.80 ± 0.02	−0.07 ± 0.08
0122+1216	4210 ± 160	46.79 ± 0.04	⋯	⋯	⋯	47.50 ± 0.04	9.47 ± 0.06	−0.1 ± 0.10
0928+5340	4408 ± 190	46.99 ± 0.1	⋯	⋯	⋯	47.70 ± 0.1	9.64 ± 0.06	−0.05 ± 0.06
1048+4407	4162 ± 357	46.97 ± 0.05	⋯	⋯	⋯	47.68 ± 0.05	9.58 ± 0.09	−0.01 ± 0.15
1335+4101	3010 ± 2200	47.06 ± 0.01	⋯	⋯	⋯	47.78 ± 0.01	9.34 ± 0.48	0.315 ± 0.50
1510+5148	4515 ± 2250	46.51 ± 0.05	⋯	⋯	⋯	47.24 ± 0.05	9.43 ± 0.36	−0.31 ± 0.41
1638+1500	3670 ± 970	47.02 ± 0.1	⋯	⋯	⋯	47.74 ± 0.1	9.50 ± 0.25	0.12 ± 0.26

Note. Here L_{bol}, M_{BH} , and $\log \lambda_{\mathrm{Edd}}$ are derived from the broad Hβ emission line, if available; otherwise, they are estimated using the Mg II emission line. The error bars of BH masses are the measurement uncertainties derived from 100 Monte Carlo simulations (not including the systematic uncertainty of the scaling relation, which typically is about 0.3 dex).

3.1. Measurements from Optical Spectra

Similar to previous studies (e.g., Grier et al. 2016; Yi et al. 2019a), we adopt a reddened power-law model to fit the continuum with a nonlinear least-squares fitting algorithm. We modeled the continuum in each spectrum using an SMC-like reddened power-law function from Pei (1992) with three free parameters, including the amplitude, power-law index, and extinction coefficient. The initial continuum fit windows are composed of relatively line-free (RLF) regions. However, these default windows do not always reasonably sample the continuum for all quasars in the sample, so they are adjusted where necessary to reach an acceptable fit. In particular, apparent emission/absorption lines present in the default windows among all spectra have been excluded.

We mask pixels flagged by "and-mask" from the SDSS pipeline before the continuum fit. All spectra are then converted to the rest frame using the redshifts determined by the [O III], Hβ, or Mg II lines from the near-IR spectra. Some emission and/or absorption features appear to be frequently present in the same fitting regions. Therefore, we adopt a sigma-clipping algorithm that consists of fitting the reddened power-law function to the RLF windows for each spectrum and then rejecting data points that deviate by more than 3σ from the continuum fit for each pixel in each window. The final continuum fit is obtained by refitting the remaining data points. We do not attach physical meaning to the values of $E(B-V)$ derived from our fits, since there is a degeneracy between the UV spectral slope and intrinsic reddening. The uncertainty of the continuum fit is obtained via a Monte Carlo approach through randomizations of spectral errors in the RLF windows. Then, quantities such as AI (C IV), minimum/maximum trough velocities, and equivalent width (EW) are measured based on the reddened power-law fits (see Table 2).

3.2. Flux Calibration of Near-IR Spectra

The near-IR spectroscopic observations were carried out under nonphotometric conditions. In addition, the cross-dispersion mode of spectroscopy may lead to a large uncertainty for near-IR spectral flux calibration, so an absolute flux calibration is required for reliable measurements of QSO properties. Since quasars usually show less variability at redder wavelengths, we use the converted photometric flux at SDSS i/z; 2MASS *J/H/K*, if it existed; and WISE 1/2 to scale the spectral flux. Although the photometric and spectroscopic data were not simultaneously observed, for simplicity, we assume no significant continuum variability between the photometric and spectroscopic epochs for all QSOs in the sample. For the BAL QSOs without *J/H/K* magnitudes in our sample, we select reference BAL QSOs with *J/H/K* magnitudes and similar optical spectral shapes to our targets from DR14. We then use the models that are best fitted for the continua of the reference QSOs to fit our targets with SDSS-i/z and WISE-1/2 magnitudes.

As an example demonstrated in Figures 1 and 2, two BAL QSOs were finally chosen as a reference to guide the local spectral energy distribution (SED) fit for the target (J120447.15 +330938.7) without near-IR photometric observations. The SEDs in the two matched BAL QSOs appear to be redder than non-BAL QSOs, most likely due to intrinsic reddening and Lyα-forest absorption at high redshift. We only account for the local SED fit between 1600 and 10000 Å in the rest frame, where a power-law or reddened power-law continuum shape is expected. A long-wavelength cut is necessary, since the hot-

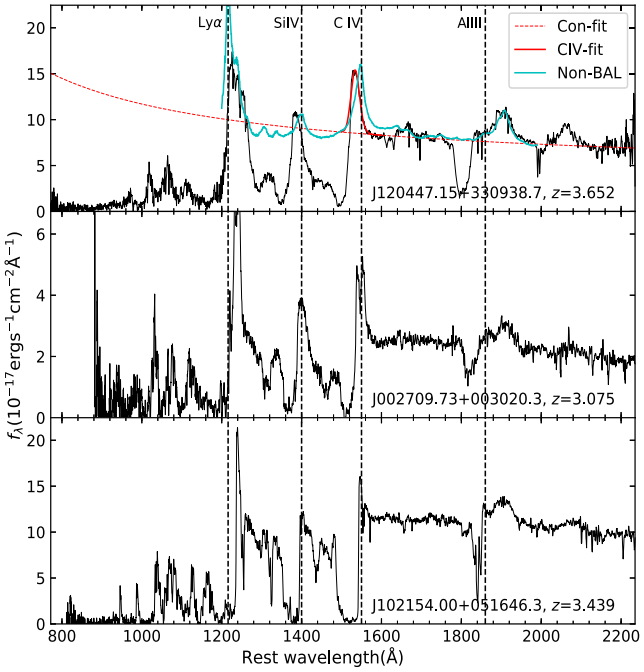

Figure 1. The top panel demonstrates continuum (red dashed) and non-BAL template (cyan) fits. The red solid line is a Gaussian fit of the C IV line. The middle/bottom panels show the matched spectra with similar redshift, AI (C IV), and spectral shape.

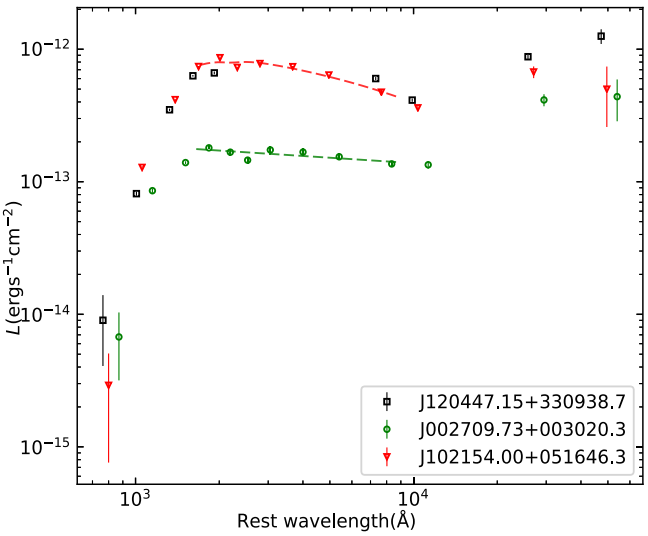

Figure 2. The SEDs of the three quasars constructed from SDSS, UKIDSS, and WISE photometric magnitudes. The dashed lines show reddened power-law (red) and power-law (green) fits for the two matched quasars between 1600 and 9000 Å.

dust reprocessing starts to dominate the QSO SED at $\lambda > 10000$ Å. The local SEDs of the two reference QSOs can be well fitted by the power-law and reddened power-law models, respectively (see Figure 2). Finally, we fit the local SED of our target using the above two models that are applied to the SED fitting process of the two reference QSOs in the same wavelength range (see Figure 3). Their differences are taken as propagated uncertainties for the placement of the continuum. As the uncertainty is dominated by the above procedures, we did not account for additional uncertainties, such as the uncertainty generated from Monte Carlo simulations.

In general, we found that the 5100 Å flux density derived from a power-law fit is quite close to that from a reddened power-law fit, while a larger deviation may appear at 3000 Å for these quasars without near-IR photometric observations in the sample. Thus, the continuum placement at 5100 Å is our preferential choice for the conversion to the bolometric luminosity using the nominal factors (5.18 for 3000 Å and 9.26 for 5100 Å, respectively; see Shen et al. 2011). Finally, the absolute flux calibration is corrected by the Galactic extinction using the Rv = 3.1 Milky Way extinction model (Cardelli et al. 1989) and a corresponding Av value (Schlafly & Finkbeiner 2011).

3.3. The Emission Line Measurements

Emission line properties are measured by fitting the local regions around the Hβ and/or Mg II emission lines with a pseudocontinuum+line model (see inset panels in Figure 3). Strong telluric absorption windows are masked out in the near-IR spectra before fitting. For consistency, we adopt a similar method of continuum fitting and emission line modeling from Schulze et al. (2017), which is illustrated as follows.

1. The continua around the Mg II and Hβ emission lines are fitted by the model including a power-law function +optical/UV Fe II template (Boroson & Green 1992; Salviander et al. 2007). We do not consider the Balmer continuum in this work.
2. The BEL fitting is then based on the pseudocontinuum-subtracted spectrum. No more than one narrow and three broad Gaussians are adopted to fit the BELs. We mask out absorption troughs during the fitting around the Mg II emission line if its profile is affected by these troughs.
3. Due to the weakness of the [O III] emission line in the sample and spectral quality, the [O III] emission line is fitted by one Gaussian for most quasars in the sample. The upper limits on [O III] blueshift and [O III] FWHM are set by 1000 and 2000 km s^{-1}, respectively, to account for possible broad [O III] components that may be associated with quasar outflows.
4. Since the widely used Boroson & Green (1992) template may fail to provide a satisfactory Fe II fit for all spectra, following Bischetti et al. (2017), we add an additional two Gaussians during the fit for those objects with strong Fe II emission at ∼4940 and ∼5040 Å, respectively.

The upper limit on the velocity width (2000 km s^{-1}) used for the [O III] line fit is obviously larger than the typical velocity width (<900 km s^{-1}) of narrow emission lines (NELs). However, this upper limit is reasonable, since the signatures of NEL outflows appear to be common in the luminous quasar population, particularly at high redshifts (e.g., Netzer et al. 2004; Harrison et al. 2014; Bischetti et al. 2017). The wavelength separation between the [O III] λ5007 and [O III] λ4960 components has been constrained to the range from 45 to 50 Å in the rest frame, with the ratio of their amplitudes constrained between 2.5:1 and 3:1. Limited by the quality of these near-IR spectra, we use only one Gaussian to fit the [O III] λ5007 emission line for the majority in the sample, except for three QSOs with apparent broad [O III] profiles and high S/Ns (J0844+0503, J1259+6101, and J1415+1129; see Figure 4). In particular, we applied two methods to decompose the plateau-like profile around the Hβ + [O III] region in J0844 +0503. One is followed by the above procedures; the other is

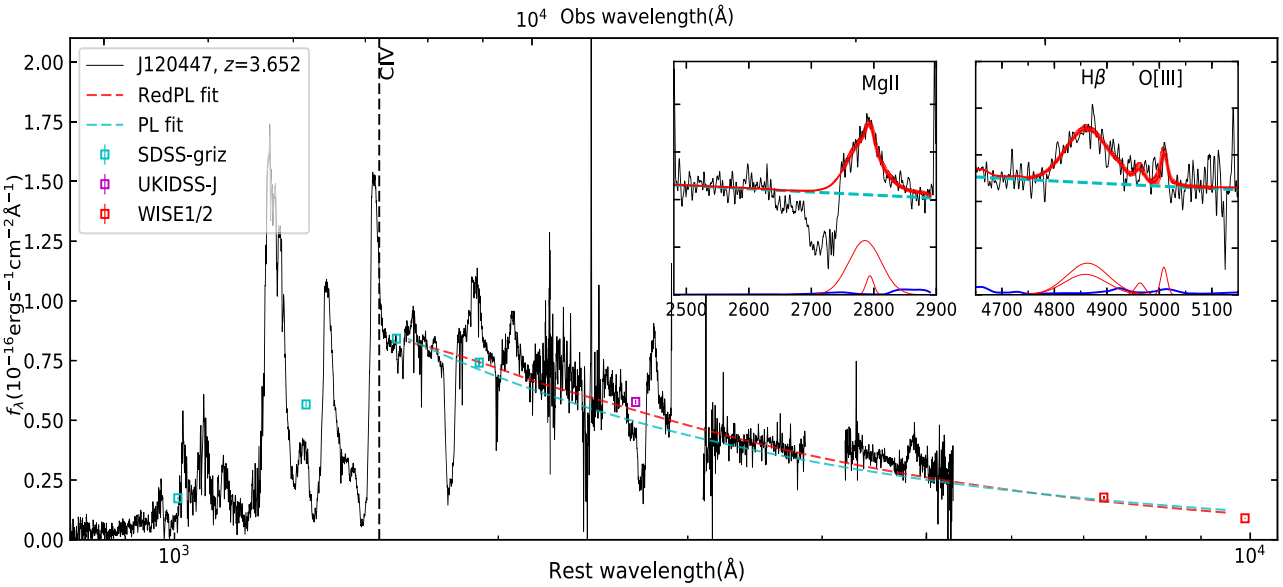

Figure 3. Example of the SED fit using power-law (PL) and reddened power-law functions based on photometric (cyan and red squares) data. The black dashed line shows an apparent blueshift compared to the systemic redshift determined by the [O III] 5007 emission line. The cyan, magenta, and red squares represent photometric data from SDSS, UKIDSS, and WISE, respectively. Inset panels show spectral fits around the Mg II and Hβ emission lines. The cyan dashed lines represent the power-law fit for the continuum, the blue lines depict the fitted UV/optical Fe II components, and the thin red lines represent all broad and narrow Gaussians for the fits around the Mg II, Hβ, and [O III] emission lines.

based on the introduction of extremely blueshifted (>1700 km s^{-1}) and broad [O III] components (e.g., Coatman et al. 2019; Perrotta et al. 2019). The two methods yield a similar [O III] EW including both narrow and broad Gaussians, but we favor the latter, since this quasar has subrelativistic BAL outflows that may affect its NEL region (e.g., Faucher-Giguère et al. 2012). For the measurement of the FWHM of the Hβ emission line, we consider all broad Gaussians (up to three components) during the fitting process.

Spectral fits around the Mg II emission line, however, are more challenging for various reasons. First, there is no available Mg II-based size–luminosity relation such as that derived from the Hβ line from reverberation mapping campaigns (e.g., Kaspi et al. 2000; Bentz et al. 2013), indicating that BH mass estimates using the Mg II line may be less reliable than those using the Hβ line. Second, the Mg II line profile is potentially affected by absorption in our sample, especially for these objects showing deep and wide C IV BAL troughs. Although the Mg II BAL troughs are generally weaker and narrower than those found in C IV, they are often attached on the Mg II emission line profile, making their identifications more difficult than those of C IV BAL troughs. Third, Popovic et al. (2019) reported that the Mg II BEL appears to originate from two subregions: one contributes to the line core that is probably virialized, and the other is associated with an emitting region characterized by outflows and inflows nearly orthogonal to the disk, which mostly contributes to the emission of the Mg II broad line wings. Fourth, whether or not one considers the narrow component during the Mg II line decomposition may significantly affect the FWHM measurement of the broad Mg II line. Other challenges arise from different recipes of the single-epoch relation used in previous studies, the possibility of Mg II emission line blueshift (cannot be determined without the aid of Hβ), and the correction for the Mg II-based BH mass (e.g., Woo et al. 2018), and these issues need to be considered as well. Therefore, some caveats must be kept in mind when using the Mg II broad line for the BH mass estimation, especially in these quasars with extremely broad Mg II emission lines (FWHM > 6000 km s^{-1}; e.g., Yi et al. 2019b) and/or strong blue asymmetric profiles in the Mg II emission line (e.g., Plotkin et al. 2015).

To mitigate the contamination of absorption and reconstruct the Mg II emission line in a reasonable sense, we mask out these absorption regions through visual inspection. The peak position of the Mg II emission line is constrained to the wavelength range between 2796 and 2803 Å. No more than one narrow and three broad Gaussian components are taken into account during the Mg II emission line fit. Since the spectral quality does not allow us to decompose the Mg II line in a reliable way, we did not exclude the narrow component for the FWHM Mg II measurement, even if it exists in some cases. Therefore, the FWHM of the Mg II emission line is determined by combining both the broad and narrow (if it exists) Gaussian components after the spectral fitting. This would not bias our statistical results, since it causes a systematic underestimation of the FWHM Mg II for each quasar in the sample.

The whole spectral fitting process for an individual object is demonstrated in Figure 3, in which we scaled the optical/near-IR spectra by a ratio between the spectral flux and the continuum fit based on the converted photometric flux. The local SED fits derived from both the power-law and reddened power-law functions are demonstrated by the cyan and red dashed lines, respectively. All of the spectral fitting results around the Mg II and/or Hβ emission lines in the sample are shown in Figure 4.

3.4. BH Mass Estimate

At high redshift, the single-epoch scaling relation is the primary method adopted to estimate BH mass in quasars. A

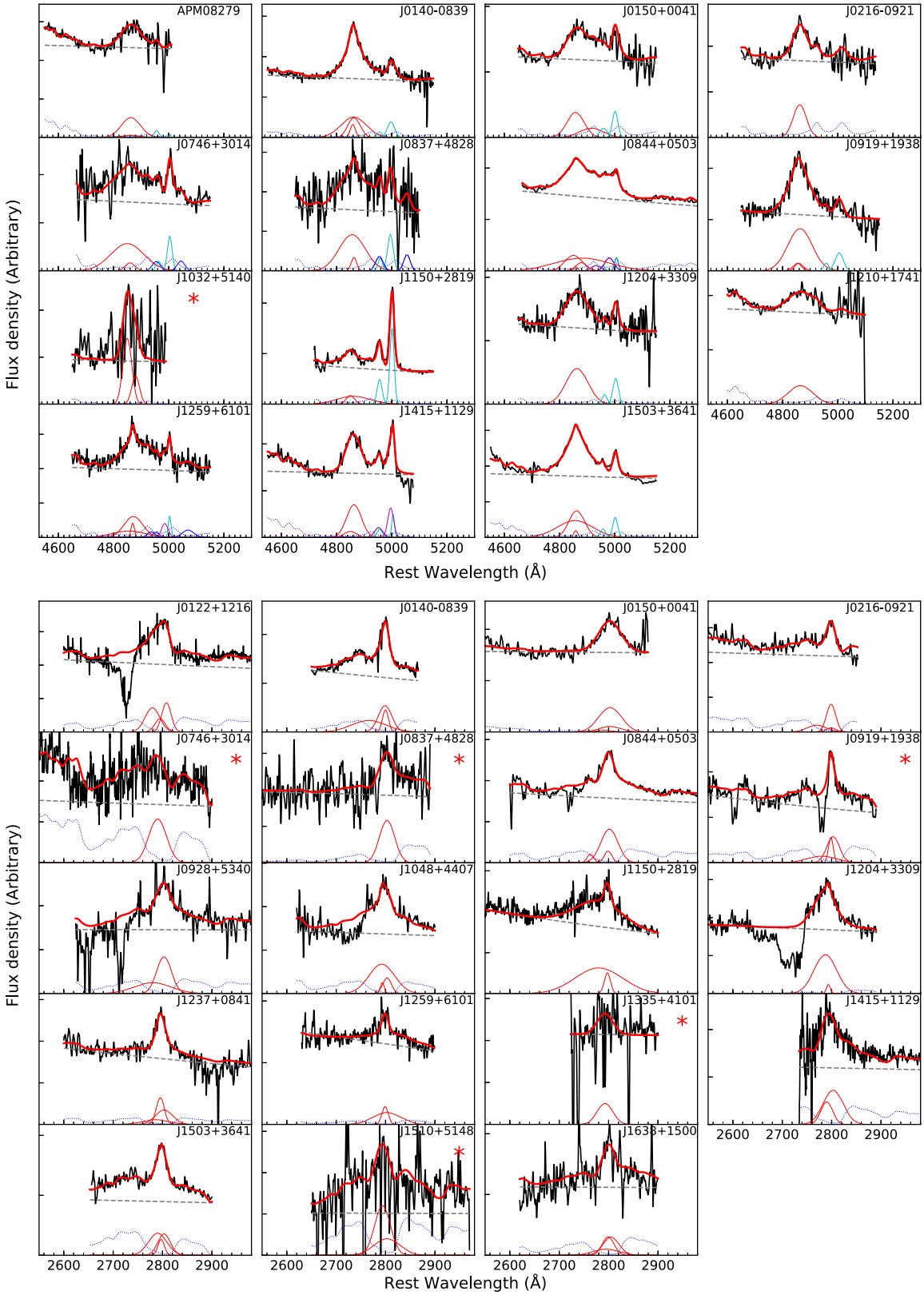

Figure 4. Spectral fits around the Hβ + [O III] (upper panel) and Mg II (lower panel) emission lines in our sample. The model of the Hβ emission line includes the power-law continuum (gray dashed), optical Fe II template (dotted blue), multiple Gaussians for the broad Hβ line (thin red), [O III] λ4960/5008 doublet (cyan and magenta lines, in which magenta lines represent broad FWHM components of the [O III] λ4960/5008 doublet lines), and an additional two broad Gaussians for Fe II bumps at 4940 and 5040 Å (solid blue), if they exist. The model of the Mg II emission line includes the power-law continuum (gray dashed), UV Fe II template (dotted blue), and multiple Gaussians for the broad Mg II line (thin red). The red asterisks refer to objects with low-S/N spectra and/or absorption attached on the line.

general equation of the relation can be expressed as follows:

$$\log\left(\frac{M_{\rm BH}}{M_\odot}\right) = a + b \times \log\left(\frac{\lambda L_\lambda}{10^{44}{\rm ergs}^{-1}}\right) + 2\log\left(\frac{\rm FWHM}{\rm kms^{-1}}\right). \quad (1)$$

There are several parameter configurations (a, b) in terms of the scaling relation from the literature (for details, see Section 3.7 in Shen et al. 2011). As a sample study, it is mandatory to adopt the same method to avoid introducing additional uncertainties for the measurements of each object. Throughout this work, for Hβ, we use the configuration of $a = 0.91$, $b = 0.5$ following Vestergaard & Peterson (2006); for Mg II, we use the configuration of $a = 0.86$, $b = 0.5$ following Vestergaard & Osmer (2009).

To quantify the measurement errors, we randomize spectral errors in the line fitting window via 100 Monte Carlo simulations and consider the standard deviation as the measurement error for each quasar. The typical measurement errors are small, only ∼0.1 dex (see Table 3). However, we do note that the main uncertainties are dominated by systematic errors, which amount to ∼0.4 dex or even higher according to previous studies (e.g., Shen et al. 2011).

3.5. The Composite Spectrum of Strong BAL QSOs

There are seven QSOs (∼32%) in our sample having strong C IV BAL features (C IV BAL EW > 60 Å) with an average S/N > 7 at 3000 or 5100 Å. All of them are LoBALs and exhibit large C IV BEL blueshifts measured by the apparent C IV BEL peak. This method yields only a lower limit on the C IV BEL blueshift due to the blueshifted BAL effect. In addition, all seven QSOs have trough velocity widths of $\Delta v > 10,000\ {\rm km\,s^{-1}}$ and BAL velocities of $v_{\rm max} > 20,000\ {\rm km\,s^{-1}}$ along our line of sight, indicating powerful nuclear outflows that may be capable of affecting their host galaxies via an energy-conserving expansion process (e.g., Faucher-Giguère et al. 2012). We thus construct a composite spectrum from these QSOs to investigate similarities and differences in the continuum and emission line properties compared with the non-BAL composite from Zuo et al. (2015) matched in luminosity and the non-BAL composite from Vanden Berk et al. (2001).

These optical/near-IR spectra used to construct the composite spectrum cover a wide wavelength range from 900 to 5500 Å in the quasar rest frame. All selected spectra are normalized at 1600 Å for the optical spectra and 3600 Å for the near-IR spectra. We use the geometric mean among these normalized spectra to produce stacked spectra as shown in Figure 5, where the composite spectra at 900 Å < λ < 1700 Å (top panel) and 1800 Å < λ < 5500 Å (bottom panel) are generated by the optical and near-IR spectra, respectively. Since the near-IR spectra of the seven BAL QSOs have different redshifts ranging from 3.179 to 4.82, the composite spectra have some breaks due to the cut of the telluric absorption windows.

The BAL composite spectrum shows significant intrinsic reddening at $\lambda < 2000$ Å, though it appears to be largely free of reddening at $\lambda > 4000$ Å. The conspicuous differences between the BAL and non-BAL composites at $\lambda_{\rm rest} < 1600$ Å could be due primarily to strong BAL absorption in C IV, Si IV, N V+Lyα, and O VI+Lyβ at a similar velocity, plus stronger intergalactic medium absorption at higher redshift. After scaling the two non-BAL composites to the BAL composite,

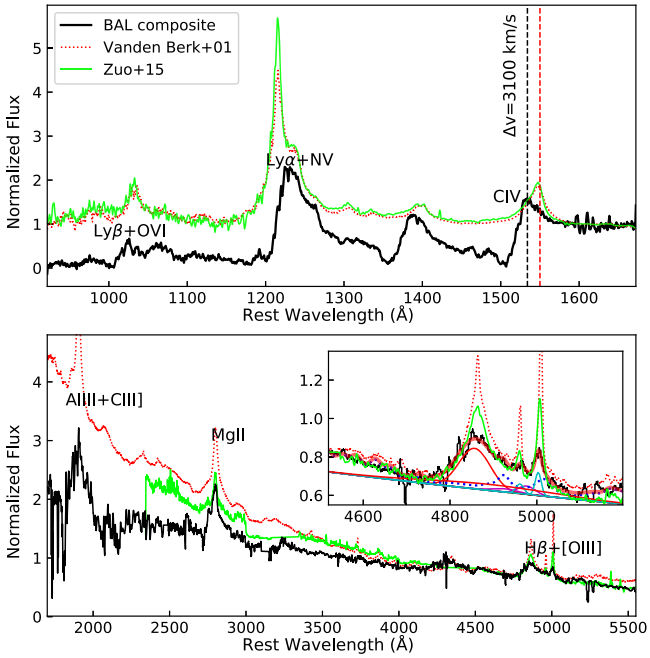

Figure 5. The black lines show the composite spectra (smoothed by a 20 pixel boxcar filter for clarity) generated from seven LoBAL QSOs from our sample at $3 < z < 5$. The green and red spectra depict the non-BAL composites from Zuo et al. (2015) and Vanden Berk et al. (2001), respectively. The vertical dashed black line shows the apparent C IV BEL blueshift with respect to [O III]. Clearly, our composite has a larger C IV BEL blueshift and weaker [O III] emission than that from Zuo et al. (2015) matched in luminosity. The inset panel shows the spectral fit around Hβ, in which different colored components have the same meaning described in the caption of Figure 4.

we found that all of them have a similar Fe II emission line profile at 4500Å < $\lambda_{\rm rest}$ < 4700 Å, suggesting that optical Fe II emission may not depend on redshift, luminosity, and the presence of outflows. After performing a spectral fit to the Hβ +[O III] region (see Figure 5), we found a narrow unshifted (cyan) and broad blueshifted [O III] doublets (magenta). In addition, the entire Hβ emission line profile can be well fitted by a single, almost unshifted Gaussian and a very broad redshifted Gaussian, supporting the idea that the Hβ emission line in BAL QSOs can serve as an equally reliable BH estimator as in non-BAL QSOs. The BAL composite shows an apparently wider Hβ emission line profile than the two non-BAL composites, probably signaling an intrinsic difference between the two quasar populations (see the separation between Populations A and B using FWHM Hβ from Sulentic et al. 2000). However, when taking a close-up look at the inset panel of Figure 5, the broadening effect of the Hβ emission line in the BAL composite appears to be caused by the lack of peaky profiles in both Hβ and [O III] compared to the two non-BAL composites. This implies that the presence of outflow may predominantly affect the NELs that originated from large-scale regions. We discuss this issue in Section 5.

In good agreement with the finding from Yi et al. (2017), our composite spectrum of strong BAL QSOs reveals a striking blueshift among all of the high-ionization BELs (∼3100 km s^{-1}, possibly higher due to the blueshifted BAL effect) and nearly black absorption troughs, which in turn provides evidence in support of outflows affecting the high-ionization BEL regions. Moreover, the composite spectrum shows significant reddening at $\lambda < 3000$ Å and weak [O III] emission. As a comparison, less than 25% of the non-BAL QSOs from

Zuo et al. (2015) matched in redshift and luminosity show comparable weakness of the [O III] emission. In addition, the average C IV BEL blueshift is ∼600 km s^{-1} from Zuo et al. (2015), within which only one quasar has a C IV BEL blueshift larger than 2000 km s^{-1} (in private communication). It is worth noting at this point that all of the above studies do not have simultaneous optical/near-IR spectroscopic data, which may potentially lead to larger uncertainties in the C IV BEL blueshift than the values given above. However, the C IV BEL blueshift could remain unchanged even if the C IV BEL flux varies dramatically from epoch to epoch (e.g., Ross et al. 2019).

4. Comparison with Other Samples

In this section, we investigate the distributions of physical properties and compare them with other non-BAL and BAL samples matched within a similar luminosity and/or redshift range to our sample.

4.1. Comparison of Direct Measurements between BAL and Non-BAL QSOs

Previous studies based on non-BAL QSO samples found that the FWHM distribution of the Mg II BEL is (linearly) correlated with that of the Hβ BEL at a high significance level (e.g., Trakhtenbrot & Netzer 2012; Zuo et al. 2015); thus, the Mg II BEL is usually considered as an alternative BH mass estimator in good agreement with the Hβ line in the non-BAL population.

There are 13 objects in our sample with simultaneous observations of the Mg II and Hβ emission lines that provide an opportunity to test whether this correlation holds in the luminous BAL QSOs at high redshift. Four quasars (marked by open red squares in the top panel of Figure 6) in our sample have relatively low-S/N spectra and/or broad absorption attached on the Mg II line, which may bias the statistical results. We checked the correlation after excluding them and found that the results are consistent with the subsample of 13 objects via the Spearman test. Therefore, we use the entire subsample of 13 BAL QSOs in our analyses below.

We choose three non-BAL comparison samples (Zuo et al. 2015; Coatman et al. 2017; and Vietri et al. 2018; hereafter Zuo15, C17, and V18, respectively) within a similar range of luminosity and redshift to our sample. The sample of Zuo15 includes 24 non-BAL QSOs at a similar redshift and luminosity to our sample, among which 22 have the coverage of both the Hβ and Mg II emission lines. The near-IR spectra from Zuo15 and our sample were obtained by the same instrument (P200/TripleSpec), largely alleviating uncertainties caused by different instruments for the comparisons. The comparison sample of C17 consists of 230 non-BAL QSOs at $1.5 < z < 4$, from which we select 19 within the same redshift and luminosity ranges to our sample ($z > 2.56$ and $46.5 < \log L_{5100} < 47.3$). Additionally, we select 13 non-BAL QSOs at $z \sim 3.3$ and $\log L_{5100} \sim 47$ from Vietri et al. (2018) to construct the V18 comparison sample.

According to the single-epoch scaling relation, the BH mass measurement is proportional to the square of FWHM and root square of monochromatic luminosity (the former is an indirect measurement depending on sophisticated analyses, as roughly mentioned in Section 3.3), and it is essential to investigate the distributions of the two quantities in our sample and compare them with other studies. As shown in the top panel of Figure 6,

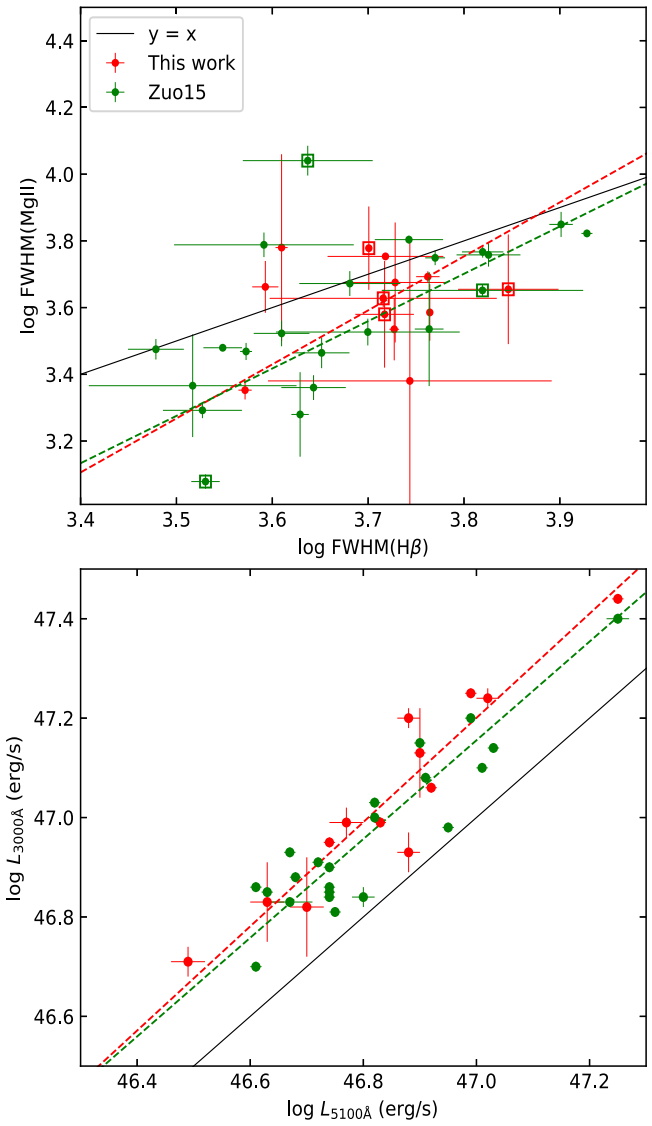

Figure 6. Top: FWHMs of Mg II vs. Hβ emission lines. The black line is the 1:1 distribution. The open red/green squares represent these objects with relatively low-quality fitting results from the two samples. Bottom: distribution of 5100 Å monochromatic luminosity vs. 3000 Å monochromatic luminosity. The red and green dashed lines are the linear fits based on the orthogonal distance regression.

the distribution of FWHM Mg II versus FWHM Hβ in this work is broadly consistent with that from Zuo et al. (2015) via orthogonal distance regression fits[10] (the red and green dashed lines are the two fits for the two samples, respectively). Although there is no significant difference in the distribution of FWHM Mg II from the two samples, as determined via a two-sample Kolmogorov–Smirnov (K-S) test ($p_{KS} = 0.23$), a difference may exist in the distribution of FWHM Hβ ($p_{KS} = 0.1$). In addition, both FWHM distributions of the two samples deviate from the one-to-one line (black), with more objects showing FWHM Hβ larger than FWHM Mg II. However, the FWHM distribution between the two different BELs from our sample is less correlated compared with Zuo15, which is confirmed via the Spearman test ($r = -0.09$, $p = 0.775$ and $r = 0.67$, $p = 0.0006$ for our sample and Zuo15, respectively). The lack of correlations in

[10] https://docs.scipy.org/doc/scipy/reference/odr.html

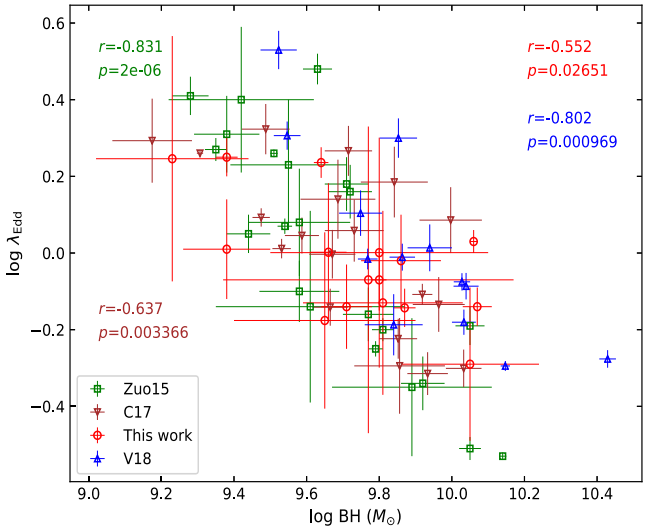

Figure 7. Distributions of Eddington ratio vs. BH mass, in which the subset of the BAL sample (red) and three non-BAL samples have a similar redshift/luminosity range. All three non-BAL samples show strong correlations compared to a tentative correlation in the BAL sample.

our sample is likely due to strong nuclear outflows traced by BALs and/or BEL blueshifts when noticing that both samples have a similar luminosity and redshift range.

Conversely, the two samples follow a similar linear relation in the distribution of 5100 versus 3000 Å monochromatic luminosity (see red/green dashed lines in the bottom panel of Figure 6). Specifically, we found strong correlations for both samples via the Spearman tests ($r = 0.92$, $p = 10^{-5}$ and $r = 0.75$, $p = 5 \times 10^{-5}$ for this work and Zuo15, respectively), which are consistent with previous studies based on non-BAL QSOs. The similarity in the luminosity relation and difference in the FWHM relation between the BAL and non-BAL samples, to some extent, support the scenario where strong BAL outflows are affecting the (Mg II) BEL regions.

4.2. Comparison of Derived Measurements with Non-BAL QSOs Matched in Luminosity and Redshift

Unlike the investigation and comparison of direct measurements in the above subsection, here we have to use derived measurements to explore the effect of outflows, due to the lack of simultaneous observations or reported Mg II and Hβ lines from the C17 and V18 studies. We use the 16 BAL QSOs at $z < 4$ from our sample and compare them with the above three non-BAL QSO samples based on near-IR spectroscopy in a similar luminosity and redshift range to our sample (see Figure 7). Based on the two-sample K-S test, there is no statistically significant difference in the distributions of Eddington ratios between the BAL and non-BAL samples; but potential differences may exist in the distribution of BH masses ($p_{KS} = 0.14$) between this work and Zuo15, tentatively hinting that the growth of SMBHs in our sample is regulated by BAL outflows. Since the K-S test is incapable of finding differences in the correlation strength between different parameters, and our sample, at first glance, appears to have no correlation in the distribution compared to apparent correlations in the other three matched comparison samples, we perform the Spearman test to quantify this difference. We found strong correlations in all three non-BAL comparison samples at a highly significant level but only a tentative correlation in our sample (see Figure 7 and Table 4).

The distributions of BH mass versus Eddington ratio above are unlikely to be biased because all of them are derived from the same BH mass estimator (Hβ), which is largely free of the effects of intrinsic reddening and absorption. Despite a small number of quasars in the four samples, the difference in the correlation strength between the non-BAL and BAL QSO samples is unlikely to be caused by the difference in sample size, as the V18 (blue) sample consisting of fewer QSOs shows an even stronger correlation than those from C17 and our sample (the number of quasars with Hβ-based BH masses in Z15, C17, V18, and this work are 22, 19, 13, and 16, respectively). Therefore, we attribute such a difference to the effects of substantial outflows traced by strong BALs and large C IV BEL blueshifts ubiquitously seen in our sample.

4.3. Comparison of Eddington Ratio with Non-BAL QSOs at Lower Luminosities

There are another two non-BAL QSO samples with available estimated BH masses and Eddington ratios at $z \sim 4.8$and $z \sim 2.4$ and 3.3 (Netzer et al. 2007; Trakhtenbrot et al. 2011). Although the two samples have a lower luminosity range, they can provide additional diagnostics for systematic comparisons between the BAL and non-BAL populations, particularly in the context of normalized accretion rate, namely Eddington ratio (λ_{Edd}).

In this subsection, we use our entire sample consisting of 22 BAL QSOs at $z > 2.5$. The BH masses from all three samples were estimated using the Hβ and Mg II emission lines at $z < 4$ and $z > 4$, respectively. Because the bolometric correction factor adopted in this work is about 1.5 times higher than that from the two non-BAL samples (see Section 5.1 from Trakhtenbrot et al. 2011), we correct the distribution of bolometric luminosities by applying the same factor to the two comparison samples. As shown in Figure 8, there is a distinct separation between different quasar samples, with a larger average BH mass in this work (this is quantitatively confirmed by a two-sample K-S test with $p_{KS} = 2 \times 10^{-8}$). The vast majority of BAL QSOs in our sample are bounded by $\log\lambda_{Edd} = -0.5$ and $\log\lambda_{Edd} = 0.5$, with a median Eddington ratio of $\log\lambda_{Edd} = -0.04$, a value that is approximately equal to that from T11. However, our sample contains BAL QSOs with significantly higher luminosities and BH masses than T11 (see Figure 8).

There are six LoBAL QSOs at $z > 4.3$ in our sample (filled red circles in Figure 8) with BH masses estimated by the Mg II emission line. We compare the distributions of Eddington ratios between these six LoBAL QSOs and those from T11 sample, as they are also measured using the Mg II BH mass estimator. Based on the two-sample K-S test, we found that the two samples are likely drawn from the same distribution of Eddington ratio ($p_{KS} = 0.9$). Therefore, our observational results together indicate that BAL QSOs, on average, do not have higher Eddington ratios than non-BAL QSOs at similar luminosity and/or redshift, supporting the argument that a high Eddington ratio is not sufficient for producing strong outflows (Stern & Laor 2005).

Table 4
Near-IR Spectroscopic Studies of BAL QSOs at $z \gtrsim 3$

	L_{5100}^{a}	L_{5100}^{b}	FWHM Hβ^{a}	FWHM Hβ^{b}	$\lambda_{\rm Edd}$
L_{3000}	(0.92, 10^{-5})	(0.75, 5 × 10^{-5})	...	...	...
FWHM Mg II	...	...	(−0.09, 0.775)	(0.67, 0.0006)	...
$M_{\rm BH}^{a}$	...	...	...	-	(0.552, 0.026)
$M_{\rm BH}^{b}$	...	...	...	...	(0.831, 2 × 10^{-6})
$M_{\rm BH}^{c}$	...	...	...	...	(−0.637, 0.003)
$M_{\rm BH}^{d}$	...	...	...	...	(−0.802, 9 × 10^{-4})

Note. Spearman test results (r, p) of direct (L_{5100} and FWHM) and derived ($M_{\rm BH}$ and $\lambda_{\rm Edd}$) measurements from different samples, in which a, b, c, d represent this work, Zuo15, C17, and V18, respectively.

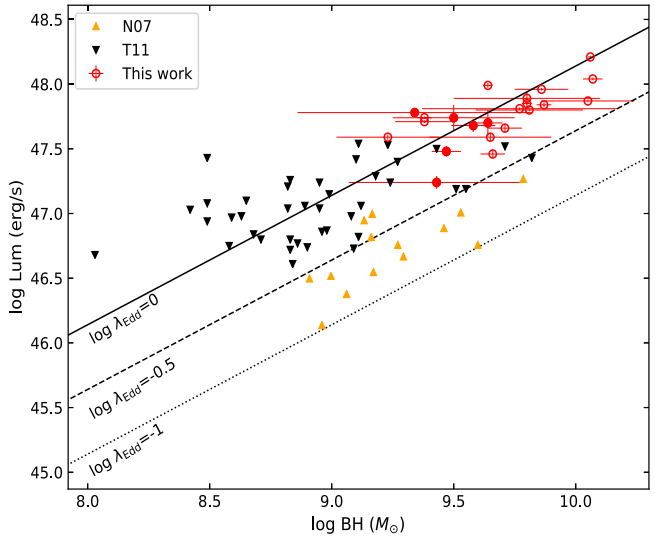

Figure 8. Distributions of bolometric luminosity vs. BH mass for the three samples, where dotted, dashed, and solid black lines represent $\log\lambda_{\rm Edd} = -1, -0.5, 0$, respectively. Filled/open red circles are the BAL QSOs at $z > 4.3$ and $z < 4$ in our sample, respectively. It is clear that BAL QSOs, on average, do not have a higher Eddington ratio compared to the lower-luminosity non-BAL sample of T11 at $z\sim$ 4.8.

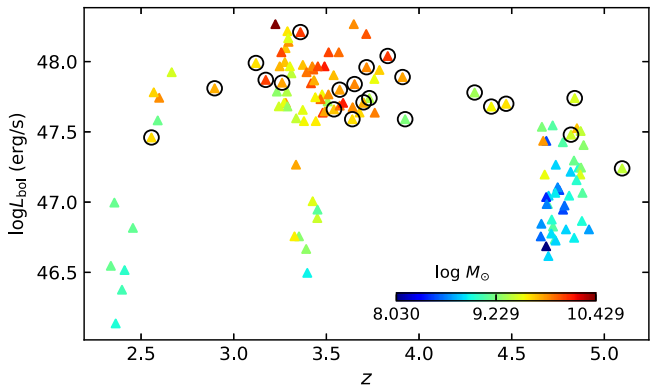

Figure 9. Distributions of redshift vs. bolometric luminosity from the BAL (triangles with overplotted circles) sample and non-BAL comparison samples constructed from Zuo15, C17, V18, N07, and T11, color-coded by BH mass.

4.4. An Overview of the BAL and Non-BAL Samples

Figure 9 presents the distribution of redshift versus bolometric luminosity from our BAL sample and the aforementioned non-BAL comparison samples. The non-BAL QSOs with bolometric luminosities less than 47.6 erg s^{-1} in the logarithmic scale are from N07 and T11, as discussed in the above section. Note that at $z < 4$, all of the bolometric luminosities and BH masses are derived by the 5100 Å continuum flux and the scaling relation for Hβ, respectively, which, in general, could provide more reliable measurements than those at $z > 4$. At fixed luminosity, we do not see any clear trends with respect to the growth of SMBHs either from our BAL sample or the augmented non-BAL samples from Zuo15, C17, V18, N07, and T11. However, limited by the sample size, we cannot draw any conclusions regarding the BH growth and redshift evolution.

5. Discussion

We present the observational results of our sample and systematic comparisons with other non-BAL samples matched in redshift and/or luminosity throughout Section 4. Here we systematically assess the role of nuclear outflows and their effects in conjunction with the reported findings from other BAL/non-BAL studies that are relevant to this work. We discuss the underlying link between BAL and BEL outflows and propose an inhomogeneous outflow system filled with different-form QSO winds along different sight lines, which can mostly explain these observational results found from the BAL and non-BAL samples.

The lack of correlation between Mg II and Hβ FWHMs, the marginal correlation between BH mass and Eddington ratio, the striking C IV BEL blueshift and nearly black C IV BAL trough seen in the composite, and, most importantly, the presence of BALs in our sample together indicate that nuclear outflows are capable of affecting their BEL regions, particularly the high-ionization BEL region. This is also supported by recent studies (e.g., Coatman et al. 2017; Vietri et al. 2018), where they found a strong correlation between C IV BEL blueshift and C IV FWHM but no correlation between C IV BEL blueshift and Hβ FWHM. Additional evidence can be found from some weak emission line quasars, among which the BEL blueshift increases dramatically from Mg II to C IV (e.g., Plotkin et al. 2015; Yi et al. 2019b), supporting the idea that nuclear outflows may exert a significant effect only on the high-ionization BELs. Combining other observational results from large sample studies, i.e., BAL QSOs, tends to have larger C IV BEL blueshift than non-BAL QSOs (e.g., Richards et al. 2011; Rankine et al. 2020); C IV BEL blueshift correlates with BAL trough velocity and width (Rankine et al. 2020); and the BAL fraction appears to increase as the increase of C IV BEL blueshift at fixed C IV BEL EW (Rankine et al. 2020). We propose that BEL blueshift and BALs could be different manifestations of the same outflow system viewed at different sight lines and/or phases. This can be easily understood because, for a bulk outflow system with different-form QSO

winds (e.g., BALs, mini-BALs, or NALs) along different sight lines, BEL blueshift can be detected along most sight lines due to the fact that each outflow unit can absorb, as well as emit, photons. As a comparison, BALs can be detected only in specific sight lines with sufficient physical conditions that allow their formation. For an individual QSO, if the BAL winds carry more material in the outflow system than other-form QSO winds, then the largest BEL blueshift is likely observed along or close to the BAL sight line (for a demonstration, see Figure 5 from Elvis 2000).

On the other hand, the [O III] weakness is known to depend on quasar luminosity (e.g., Sulentic et al. 2004; Stern & Laor 2005, 2012). Previous studies also found that the [O III] weakness tends to be associated with C IV BEL blueshift based on the investigations of luminous non-BAL QSOs (e.g., Netzer et al. 2004; Vietri et al. 2018). As a comparison, the BAL composite characterized by a striking C IV BEL blueshift and weak [O III] emission suggests that the [O III] weakness is more strongly correlated with the C IV BEL blueshift than with luminosity, given that our sample has a similar luminosity range to the non-BAL sample of Zuo15. Intriguingly, this is in good agreement with Coatman et al. (2019), where they found a much stronger anticorrelation between C IV BEL blueshift and [O III] EW than between C IV BEL blueshift and bolometric luminosity from a sample consisting of 213 non-BAL QSOs at $2 < z < 4$. Although large C IV BEL blueshift is most likely caused by nuclear outflows, other possibilities cannot be firmly ruled out either (e.g., Gaskell 1982). Unlike the non-BAL sample studies mentioned above, BALs are unambiguously produced from nuclear outflows. Therefore, our investigations of the relation between C IV BEL blueshift and [O III] emission among BAL QSOs provide complementary and compelling evidence in support of the presence of nuclear outflows affecting the NEL regions, which are notably characterized by the lack of NEL profiles as shown in Figure 5. Observationally, the strong anticorrelation between C IV BEL blueshift and [O III] emission (Coatman et al. 2019), as well as the colocation of BAL and non-BAL QSOs as a function of C IV BEL and other physical properties (Rankine et al. 2020), together support our argument that BAL and BEL blueshift could be different manifestations of the same nuclear outflow system viewed at different sight lines and/or phases. In this scenario, it is naturally expected that the presence of substantial nuclear outflows traced either by strong BALs or large BEL blueshifts can block a significant amount of ionizing photons from reaching the NEL region and/or sweep away the NEL gas, hence leading to weak [O III] emission regardless of a specific orientation. This can be tested from individual QSOs in the future.

Last but not least, if these high-z BAL QSOs have the biconical NEL regions often seen in low-z AGNs (e.g., Liu et al. 2013), our investigations would imply a wide opening-angle scenario for the presence of different-form QSO winds in the same outflow system, which is filled with inhomogeneous absorbers characterized by stratified density/ionization and possibly clumpy structures (e.g., Hamann et al. 2019; Yi et al. 2019b). In addition, HiBALs tend to have higher reddening and column densities than non-BALs, while LoBALs have even higher reddening and column densities than HiBALs (e.g., Reichard et al. 2003a), implying that dust could be associated with BAL outflows. Conceivably, BAL transitions among LoBAL, HiBAL, and non-BAL states tend to occur within a timescale of typically less than 5 yr in the quasar rest frame (e.g., Filiz et al. 2012; McGraw et al. 2017; Rogerson et al. 2018; Yi et al. 2019a). These observational results support an inhomogeneous, dusty outflow system rather than a simple thin-shell outflow system filled with homogeneous absorbers. However, the detailed investigation of such an outflow system requires a significantly large BAL sample based on optical/near-IR spectroscopy to cover both C IV and Hβ, dedicated observations of individual quasars with the presence of substantial outflows, and suitable modelings, which are beyond the scope of this work.

6. Conclusion and Future Work

High-redshift BAL QSOs are rare and have been studied sparsely, usually only including individual objects or very small samples. In this work, we present the largest sample study (to our knowledge) based on 22 high-redshift BAL QSOs via optical/near-IR spectroscopy. Due to the lack of a similar sample study based on high-z BAL QSOs in the literature, we compared them with non-BAL QSOs matched in luminosity and/or redshift, mainly focusing on the investigations of nuclear outflows and their effects. Our main results are concluded as follows.

1. We identified 12 LoBAL QSOs in this sample, and the fraction ($\sim$54%) is significantly higher than that from low-z samples (typically $\sim$10%). This is likely caused by our preferential selection of strong BAL QSOs in constructing the sample (Section 2.1).
2. We construct the composite spectra using seven BAL QSOs with the presence of subrelativistic outflows, from which we see the prevalence of large C IV emission line blueshift ($\sim$3100 km s^{-1}) and weak [O III] emission. In combination with the same trend found from non-BAL samples, our investigations provide complementary and compelling evidence that the presence of nuclear outflows in a QSO is indeed capable of affecting its NEL region (see Section 3.5).
3. In the BAL sample, the 3000 and 5000 Å continuum luminosities show a strong correlation, consistent with previous non-BAL QSO studies; however, there is no correlation between the Mg II and Hβ lines in FWHM, likely due to the effect of nuclear outflows traced by BALs and C IV BEL blueshifts. Together with the striking features shown in the composite constructed from the seven LoBAL QSOs, our investigations offer strong evidence for nuclear outflows influencing the BEL regions (see Section 4.1).
4. In the distribution of BH mass versus Eddington ratio, our sample shows only a tentative correlation at a marginally significant level compared to strong correlations at highly significant levels from the three non-BAL comparison samples matched in luminosity and redshift, again possibly due to an outflow effect in our sample (see Section 4.2).
5. Our observational results indicate that these high-redshift BAL QSOs, on average, do not have a higher Eddington ratio than that from non-BAL QSOs matched in luminosity and/or redshift (see Section 4.3).
6. We propose that BAL and BEL blueshift could be different manifestations of the same outflow system

viewed at different sight lines and/or phases (see Section 5).

Our systematic investigations of the similarities and differences between BAL and non-BAL QSOs at high redshift allow us to explore nuclear outflows and their effects from a statistical view. We propose that strong BAL and large C IV BEL blueshifts trace the same outflow system, which, in turn, can explain the striking C IV BEL blueshift in the BAL sample, as well as the prevalence of large C IV BEL blueshift and weak [O III] emission found from both the BAL and non-BAL samples. The BALs are widely accepted as smoking-gun signatures of quasar winds; therefore, our observational results provide complementary insight into the different manifestations of ionized outflows and offer strong evidence in support of these outflows affecting the BEL and NEL regions.

We leave the systematic investigation of LoBAL QSOs regarding the optical Fe II strength, luminosity, Eddington ratio, C IV BEL blueshift, [O III] strength, etc. to another dedicated work in combination with two uniform LoBAL samples at $z < 1$ (Yi et al. 2019a) and $1 < z < 2.5$ (Schulze et al. 2017). A substantially large sample of high-z LoBAL QSOs is required to investigate the redshift evolution of this population. However, it could be difficult to obtain a significantly large sample of high-z BAL QSOs in a couple of years due to their rarity, as well as the challenge of IR spectroscopy. Our spectroscopic investigations of BAL outflows and their effects based on optical/near-IR spectroscopy therefore deliver the best statistical results of high-z BAL QSOs to date. In addition, we also plan to investigate individual BAL QSOs showing extreme or peculiar phenomena, aiming to locate outflow distances, constrain outflow structures and physics, or explore the detailed process of how nuclear outflows influence the large-scale regions, which might be achieved via multi-epoch/wavelength observations and spatially resolved spectroscopy, particularly with the aid of adaptive optics or future facilities like the James Webb Space Telescope. Such investigations will greatly improve our understanding of quasar winds and their effects in the context of quasar feedback.

We thank Tinggui Wang for stimulating discussions in this work. We acknowledge the support of the staff of the Lijiang 2.4 m telescope (LJT). Funding for the telescope has been provided by CAS and the People's Government of Yunnan Province. This research uses data obtained through the Telescope Access Program (TAP), which has been funded by the National Astronomical Observatories of China, the Chinese Academy of Sciences (the Strategic Priority Research Program "The Emergence of Cosmological Structures" grant No. XDB09000000), and the Special Fund for Astronomy from the Ministry of Finance. Observations obtained with the Hale Telescope at Palomar Observatory were obtained as part of an agreement between the National Astronomical Observatories, the Chinese Academy of Sciences, and the California Institute of Technology.

W.Y. is thankful for the financial support from the program of the China Scholarships Council (No. 201604910001) for his postdoctoral study at the Pennsylvania State University. W.Y. is also thankful for the support from the National Science Foundation of China (NSFC-11703076) and the West Light Foundation of the Chinese Academy of Sciences (Y6XB016001). X.W. is thankful for the support from the National Key R&D Program of China (2016YFA0400703) and the National Science Foundation of China (11533001 & 11721303). This work is also supported by the Joint Research Fund in Astronomy (U1631127) under a cooperative agreement between the National Science Foundation of China and the Chinese Academy of Sciences.

ORCID iDs

Weimin Yi https://orcid.org/0000-0001-9314-0552
Wenwen Zuo https://orcid.org/0000-0002-4521-6281
Jinyi Yang https://orcid.org/0000-0001-5287-4242
Feige Wang https://orcid.org/0000-0002-7633-431X
John Timlin https://orcid.org/0000-0001-8131-1801
Catherine Grier https://orcid.org/0000-0001-9920-6057
Xue-Bing Wu https://orcid.org/0000-0002-7350-6913
Xiaohui Fan https://orcid.org/0000-0003-3310-0131

References

Allen, J. T., Hewett, P. C., Maddox, N., Richards, G. T., & Belokurov, V. 2011, MNRAS, 410, 860
Becker, R. H., White, R. L., Gregg, M. D., et al. 2000, ApJ, 538, 72
Bentz, M. C., Denney, K. D., Grier, C. J., et al. 2013, ApJ, 767, 149
Bischetti, M., Piconcelli, E., Vietri, G., et al. 2017, A&A, 598, 122
Boroson, T. A., & Green, R. F. 1992, ApJS, 80, 109
Brotherton, M. S., Tran, H. D., Becker, R. H., et al. 2001, ApJ, 546, 775
Coatman, L., Hewett, P. C., Banerji, M., et al. 2017, MNRAS, 465, 2120
Coatman, L., Hewett, P. C., Banerji, M., et al. 2019, MNRAS, 486, 5335
Cushing, M. C., Vacca, W. D., & Rayner, J. T. 2004, PASP, 116, 362
DiPompeo, M. A., Brotherton, M. S., Becker, R. H., et al. 2010, ApJ, 189, 83
Elvis, M. 2000, ApJ, 545, 63
Fan, Y. F., Bai, J. M., Zhang, J. J., et al. 2015, RAA, 15, 918
Farrah, D., Urrutia, T., Lacy, M., et al. 2010, ApJ, 717, 868
Farrah, D., Urrutia, T., Lacy, M., et al. 2012, ApJ, 745, 178
Faucher-Giguère, C.-A., Quataert, E., & Murray, N. 2012, MNRAS, 420, 1347
Filiz, Ak, N., Brandt, W. N., Hall, P. B., et al. 2012, ApJ, 757, 114
Gallerani, S., Maiolino, R., Juarez, Y., et al. 2010, A&A, 523, 85
Gaskell, C. M. 1982, ApJ, 263, 79
Gibson, R. R., Jiang, L., Brandt, W. N., et al. 2009, ApJ, 692, 758
Grier, C. J., Brandt, W. N., Hall, P. B., et al. 2016, ApJ, 824, 130
Hamann, F., Herbst, H., Paris, I., & Capellupo, D. 2019, MNRAS, 483, 1808
Harrison, C. M., Alexander, D. M., Mullaney, J. R., & Swinbank, A. M. 2014, MNRAS, 441, 3306
Hewett, P. C., & Foltz, C. B. 2003, AJ, 125, 1784
Irwin, M. J., Ibata, R. A., Lewis, G. F., & Totten, E. J. 1998, ApJ, 505, 529
Jeon, Y., Im, M., Kim, D., et al. 2017, ApJS, 231, 16
Jiang, L., Fan, X., Vestergaard, M., et al. 2007, AJ, 134, 1150
Kaspi, S., Smith, P. S., Netzer, H., et al. 2000, ApJ, 533, 631
Liu, G., Zakamska, N., Greene, J. E., et al. 2013, MNRAS, 436, 2576
López, S., D'Odorico, V., Ellison, S. L., et al. 2016, A&A, 594, 91
Magain, P., Surdej, J., Swings, J.-P., Borgeest, U., & Kayser, R. 1988, Natur, 334, 325
Maiolino, R., Oliva, E., Ghinassi, F., et al. 2004, A&A, 420, 889
Margala, D., Kirkby, D., Dawson, K., et al. 2016, ApJ, 831, 157
McGraw, S. M., Brandt, W. N., Grier, C. J., et al. 2017, MNRAS, 469, 3163
McLure, R. J., & Dunlop, J. S. 2004, MNRAS, 352, 1390
Netzer, H., Lira, P., Trakhtenbrot, B., Shemmer, O., & Cury, I. 2007, ApJ, 671, 1256
Netzer, H., Shemmer, O., Maiolino, R., et al. 2004, ApJ, 614, 558
Pâris, I., Petitjean, P., Ross, N., et al. 2017, A&A, 597, 79
Pei, Yichuan C. 1992, ApJ, 395, 130
Perrotta, S., Hamann, F., Zakamska, N. L., et al. 2019, MNRAS, 488, 4126
Plotkin, R. M., Shemmer, O., Trakhtenbrot, B., et al. 2015, ApJ, 805, 123
Popovic, L. C., Kovacevic-Dojcinovic, J., & Marceta-Mandic, S. 2019, MNRAS, 484, 3180
Rankine, A. L., Hewett, P. C., Banerji, M., et al. 2020, MNRAS, 492, 4553
Reichard, T. A., Richards, G. T., Hall, P. B., et al. 2003a, AJ, 126, 2594
Reichard, T. A., Richards, G. T., Schneider, D. P., et al. 2003b, AJ, 125, 1711
Richards, G. T., Kruczek, N. E., & Gallagher, S. C. 2011, AJ, 141, 167
Rogerson, J. A., Hall, P. B., Ahmed, N. S., et al. 2018, ApJ, 862, 22
Ross, N. P., Graham, M. J., Calderone, G. C., et al. 2019, arXiv:1912.05310v1
Salviander, S., Shields, G. A., Gebhardt, K., & Bonning, E. W. 2007, ApJ, 662, 131

Schlafly, E. F., & Finkbeiner, D. P. 2011, ApJ, 737, 103
Schulze, A., Schramm, M., Zuo, W., et al. 2017, ApJ, 848, 104
Shen, Y., Richards, G. T., Strauss, M. A., et al. 2011, ApJS, 194, 45
Stern, J., & Laor, A. 2005, MNRAS, 358, 1043
Stern, J., & Laor, A. 2012, MNRAS, 426, 2703
Sulentic, J. W., Marziani, P., & Dultzin-Hacyan, D. 2000, ArA&A, 38, 521
Sulentic, J. W., Stirpe, G. M., Marziani, P., et al. 2004, A&A, 423, 121
Trakhtenbrot, B., & Netzer, H. 2012, MNRAS, 427, 3081
Trakhtenbrot, B., Netzer, H., Lira, P., & Shemmer, O. 2011, ApJ, 730, 7
Trump, J. R., Hall, P. B., Reichard, T., et al. 2006, ApJS, 165, 1
Vanden Berk, D. E., Richards, G. T., Bauer, A., et al. 2001, AJ, 122, 549
Vestergaard, M., & Osmer, P. S. 2009, ApJ, 699, 800
Vestergaard, M., & Peterson, B. M. 2006, ApJ, 641, 689
Vietri, G., Piconcelli, E., Bischetti, M., et al. 2018, A&A, 617, 81
Voit, G. M., Weymann, R. J., & Korista, K. T. 1993, ApJ, 413, 95
Wang, F., Fan, X., Yang, J., et al. 2018, ApJL, 869, 9
Wang, Feige, Wu, Xue-Bing, Fan, X., et al. 2016, ApJ, 819, 24
Weymann, R. J., Morris, S. L., Foltz, C. B., & Hewett, P. C. 1991, ApJ, 373, 23
Wilson, J. C., Henderson, C. P., Herter, T. L., et al. 2004, Proc. SPIE, 5492, 1295
Woo, J.-H., Le, H. A. N., Karouzos, M., et al. 2018, ApJ, 859, 138
Yi, W., Brandt, W. N., Hall, P. B., et al. 2019a, ApJS, 242, 28
Yi, W., Green, R. F., Bai, J.-M., et al. 2017, ApJL, 838, 135
Yi, W., Vivek, M., Brandt, W. N., et al. 2019b, ApJL, 870, 25
Yi, W., Wu, X., Wang, F., et al. 2015, SCPMA, 58, 5685
Zuo, W., Wu, X.-B., Fan, X., et al. 2015, ApJ, 799, 189